On the remote sensing of oceanic and atmospheric convection in the Greenland Sea by synthetic aperture radar

Roland Romeiser,[1] Susanne Ufermann,[2] Alexei Androssov,[1] Henning Wehde,[1,3] Leonid Mitnik,[4] Stefan Kern,[1] and Angelo Rubino[1,5]

[1]   In this paper we discuss characteristic properties of radar signatures of oceanic and atmospheric convection features in the Greenland Sea. If the water surface is clean (no surface films or ice coverage), oceanic and atmospheric features can become visible in radar images via a modulation of the surface roughness, and their radar signatures can be very similar. For an unambiguous interpretation and for the retrieval of quantitative information on current and wind variations from radar imagery with such signatures, theoretical models of current and wind phenomena and their radar imaging mechanisms must be utilized. We demonstrate this approach with the analysis of some synthetic aperture radar (SAR) images acquired by the satellites ERS-2 and RADARSAT-1. In one case, an ERS-2 SAR image and a RADARSAT-1 ScanSAR image exhibit pronounced cell-like signatures with length scales on the order of 10–20 km and modulation depths of about 5–6 dB and 9–10 dB, respectively. Simulations with a numerical SAR imaging model and various input current and wind fields reveal that the signatures in both images can be explained consistently by wind variations on the order of ±2.5 m/s, but not by surface current variations on realistic orders of magnitude. Accordingly, the observed features must be atmospheric convection cells. This is confirmed by visible typical cloud patterns in a NOAA AVHRR image of the test scenario. In another case, the presence of an oceanic convective chimney is obvious from in situ data, but no signatures of it are visible in an ERS-2 SAR image. We show by numerical simulations with an oceanic convection model and our SAR imaging model that this is consistent with theoretical predictions, since the current gradients associated with the observed chimney are not sufficiently strong to give rise to significant signatures in an ERS-2 SAR image under the given conditions. Further model results indicate that it should be generally difficult to observe oceanic convection features in the Greenland Sea with ERS-2 or RADARSAT-1 SAR, since their signatures resulting from pure wave-current interaction will be too weak to become visible in the noisy SAR images in most cases. This situation will improve with the availability of future high-resolution SARs such as RADARSAT-2 SAR in fine resolution mode (2004) and TerraSAR-X (2005), which will offer significantly reduced speckle noise fluctuations at comparable spatial resolutions and thus a much better visibility of small image intensity variations on spatial scales on the order of a few hundred meters.   *INDEX TERMS:* 3314 Meteorology and Atmospheric Dynamics: Convective processes; 4275 Oceanography: General: Remote sensing and electromagnetic processes (0689); 4279 Oceanography: General: Upwelling and convergences; 4255 Oceanography: General: Numerical modeling; *KEYWORDS:* convection, Greenland Sea, remote sensing

[1]Institute of Oceanography, Center for Marine and Climate Research, University of Hamburg, Hamburg, Germany.
[2]Laboratory for Satellite Oceanography, Southampton Oceanography Centre, Southampton, UK.

[3]Now at Institute for Coastal Research, GKSS Research Center, Geesthacht, Germany.
[4]Department of Satellite Oceanography, Pacific Oceanological Institute, Far Eastern Branch of the Russian Academy of Sciences, Vladivostok, Russia.
[5]Also at Dipartimento di Scienze Ambientali, Universitá Ca'Foscari, Venice, Italy.

1. Introduction

[2] Open-ocean deep convection plays a major role for the world's oceans since it feeds the thermohaline circulation and renews the deep waters [*Broecker*, 1991]. It is geographically confined to four regions around the world, located mainly at high latitudes: Greenland, Labrador, Mediterranean, and Weddell Seas. Moreover, deep convection only takes place during winter months (see the paper by *Marshall and Schott* [1999] for a full review on open-ocean convection). Despite this well-established knowledge, conventional oceanographic methods are not well suited for the monitoring of open-ocean deep convection due to the remoteness of the geographical regions at which it occurs, adverse weather conditions, and the relatively small spatial scales of the process.

[3] The open-ocean deep convection process has often been divided into three phases: the preconditioning phase, the violent mixing phase, and the sinking and spreading phase. Preconditioning takes place in autumn/early winter, when the shallow summer thermocline is eroded and a near-surface layer has been homogenized. Additional atmospheric forcing during winter leads to the violent mixing phase, which is characterized by strong overturning of the water column through convective cells (plumes). In concert, the plumes are thought to rapidly mix properties over the preconditioning site, forming a deep mixed patch, ranging in scale from kilometers to above 100 km. In former investigations, these mixed patches were called "chimney" [*MEDOC Group*, 1970; *Morawetz et al.*, 1996; *Wadhams et al.*, 2002b], which is somehow misleading, because there is little vertical flux within such a chimney. Nevertheless, with time the horizontal gradients increase between the dense waters within the features and the ambient waters, causing baroclinic instabilities to develop at the edge of the mixed patches. This results in spreading of the dense waters and a gradual restratification of the well-mixed convective region by the stratified ambient waters. Timescales of this process are on the order of weeks to months [*Marshall and Schott*, 1999], but longer-lived features have also been observed within the Greenland Sea [*Wadhams et al.*, 2002b]. Thus the understanding of the physical processes in the Greenland Sea and their impact on the thermohaline circulation of the world's oceans could benefit greatly from a weather-independent, large-scale monitoring method like spaceborne imaging radar in support of conventional oceanographic methods.

[4] Results of previous theoretical investigations on radar signatures of open-ocean deep convection features indicate that oceanic convection cells (plumes) can produce significant signatures in synthetic aperture radar (SAR) images of the ocean [*Fischer et al.*, 1999]. Favorable conditions were found to be strong atmospheric forcing (surface heat flux on the order of 400 W/m^2) and low wind speeds, resulting in shear rates of about 2.5×10^{-3} s^{-1} and corresponding SAR modulation depths of up to $1-3$ dB. Nonetheless, to our knowledge, no such signatures have been found in actual SAR images to date. In the context of estimating the impact of open-ocean deep convection on the thermohaline circulation, it is of great relevance to investigate in more detail under what conditions signatures of mixed patches or chimneys can become visible in SAR images.

[5] In this work we present SAR images of two different scenarios in the Greenland Sea from two spaceborne sensors. One set of images exhibits mottled signatures showing some similarities to signatures reported to originate from atmospheric convection cells [cf. *Mitnik*, 1992; *Ufermann and Romeiser*, 1999b]. For the quantitative interpretation of such signatures and their inversion into wind or current variations, it is vital to determine the atmospheric or oceanic origin of the processes causing them. We show by various means that the observed signatures can only result from the presence of atmospheric convection cells, not from oceanic ones. In the second test case, the presence of an oceanic convective chimney is obvious from in situ data, but an available coincident SAR image does not exhibit any visible signatures of it. We show by numerical simulations that this is consistent with theory, since the SAR signatures to be expected from the observed feature are too weak to become visible in the existing imagery. Finally, we discuss the potential of recent and upcoming dual-polarization and high-resolution spaceborne SARs to detect oceanic convection features in the Greenland Sea and to identify and interpret SAR signatures of oceanic and atmospheric convection features unambiguously.

[6] Throughout all investigations, we assume that the water surface is not covered by ice or surface films, thus SAR signatures can only result from a modulation of the surface wave spectrum by spatially varying currents or winds, not by tracer effects. As discussed, for example, by *Johannessen et al.* [1994] and by *Carsey and Roach* [1994], oceanic convection features can also become visible in SAR images via a modulation of pancake ice or surface film concentrations. The resulting patterns can be interpreted as streamlines of the surface current field. This imaging mechanism is more direct than the clean-water imaging mechanism considered here, where image intensity variations reflect variations of the surface roughness. However, during the winter months, when the biological productivity is low and wind speeds are high, and at some distance from the ice edge, the water surface should usually be clean. The interpretation of SAR signatures observed under such conditions is a quite relevant problem.

[7] The paper is structured as follows: In the following section, the SAR images of the Greenland Sea to be examined are presented. In section 3, we demonstrate two different approaches for the interpretation of the observed SAR signatures, we show that the signatures are consistent with theoretical model results, and we present simulated SAR images of oceanic convection features as seen by various spaceborne SAR configurations. Finally, we summarize our main conclusions in section 4.

2. SAR Images of the Greenland Sea

[8] Out of a number of SAR images of the Greenland Sea which are available to us, we have selected three particularly interesting ones of two different scenarios. These will be presented in the following. The coverage of the test area by the three SAR images and by a subscene of an AVHRR image which will be discussed in section 3 is depicted in Figure 1.

2.1. Images of a Scenario With Strong Convection Cell Signatures but Unknown Oceanic Conditions

[9] Within 5 hours on 10 April 1999, the satellites ERS-2 and RADARSAT-1 acquired two SAR images of the Green-
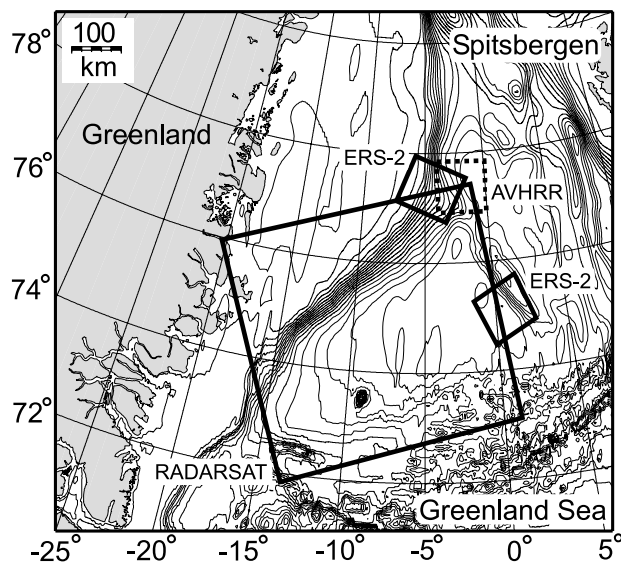
Figure 1. Map of the test area in the Greenland Sea, showing the coverage of the ERS-2 SAR images of Figure 2 (upper small solid square) and Figure 6 (lower small solid square), the RADARSAT-1 ScanSAR image of Figure 3 (large solid square), and the 100 km × 100 km subscene of an AVHRR image which is shown in Figure 11 (small dashed square).

land Sea which exhibit clear signatures of convection features. These images are shown in Figures 2 and 3. ERS-2 and RADARSAT-1 use the same radar frequency (5.3 GHz, i.e., C band), but different polarizations (ERS: VV; RADARSAT: HH) and incidence angles ($20°-26°$; $20°-50°$). Furthermore, the two images of the Greenland Sea were acquired with different look directions ($308°$ and $73°$ with respect to north). Also the sizes and resolutions of the images are quite different (ERS SAR: 100 km × 100 km at 25-m resolution; RADARSAT-1 "ScanSAR Wide" mode: 500 km × 500 km at 100 m). However, as can be seen from Figure 1, a small region in the upper right (northeast) corner of the RADARSAT ScanSAR image of Figure 3 is also covered by the ERS SAR image of Figure 2. Both images exhibit pronounced mottled, cell-like signatures in this area, which very likely originate from oceanic or atmospheric convection cells. The signatures have roughly elliptic shapes with major and minor axis lengths of about $20-25$ km and $10-20$ km, respectively, and are basically oriented in north-south direction. High-resolution in situ data of winds or currents for this scenario are not available to us.

[10] For further analysis, we have selected a large cell signature in this region from each of the two images. Both signatures were cut out of the full images, rotated such that the vertical axis is parallel to the north-south direction, smoothed, and normalized by the respective mean value of the normalized radar backscattering cross section (NRCS). They are shown with the same orientation and scaling and with comparable gray level contours separated by 1 dB in Figure 4.

[11] The observed total modulation depths (intensity ratios between the brightest and darkest parts of the signatures) are about 5.9 dB in the ERS SAR image and 9.8 dB

in the RADARSAT ScanSAR image. Although we cannot expect that both SAR signatures result from exactly the same oceanic or atmospheric feature (typical lifetimes of atmospheric convection cells would be on the order of 30 min to 2 hours) and that the oceanic and atmospheric conditions have not changed at all during the 5 hours between the acquisition times of the two images (ERS-2: 1237 UTC; RADARSAT-1: 1740 UTC), we will assume similar conditions and try to determine parameters of an oceanic or atmospheric feature which could give rise to both observed radar signatures consistently.

2.2. Images of a Well-Monitored Oceanic Convection Scenario With Invisible Radar Signatures

[12] During a cruise with RV *Lance* in the Greenland Sea in late February 2002, a strong oceanic convection feature was detected at approx. 74.95°N, 0.15°W and probed by in situ instruments [*Wadhams et al.*, 2002a]. The measured convective mixed layer depths (CMLD) shown in Figure 5 indicate the presence of a convective chimney with a diameter of about 6 km on 26 February 2002.

[13] On the same day a SAR image of the test area was acquired by ERS-2. This image is shown in Figure 6. The convective chimney should be located near the center of the left-hand border of the image, but no particular SAR signatures which could be associated with it are visible in this region. According to the ship measurements, the net heat loss of the ocean over the chimney at the time of the ERS-2 overpass was $\sim$190 W/m^2 (based on a bulk flux estimate). The wind speed in the test area was about 15 m/s,
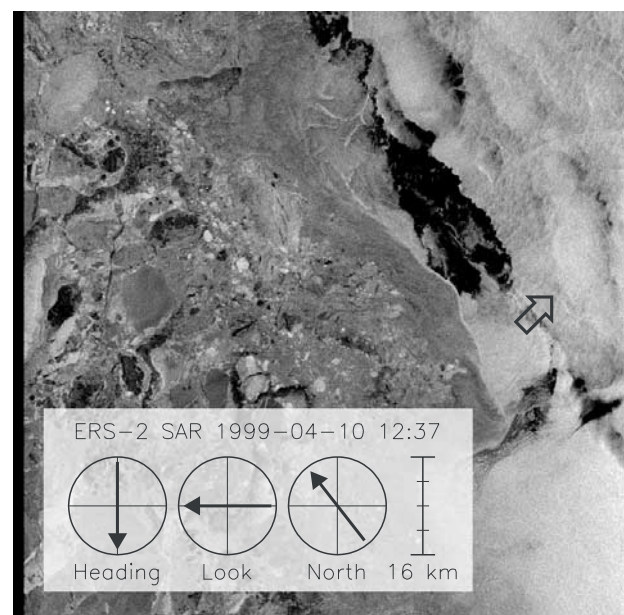

Figure 2. ERS-2 SAR image of a scenario in the Greenland Sea with pronounced signatures of convection features, 10 April 1999, 1237 UTC. Imaged area = 100 km × 100 km, full resolution = 25 m (pixel size = 12.5 m × 12.5 m), 5.3 GHz, VV, incidence angle = $20°-26°$ (near range/far range). Image intensities have been corrected (empirically) for variation with incidence angle. The arrow on the right indicates the location of the feature shown in Figure 4. © ESA 1999.
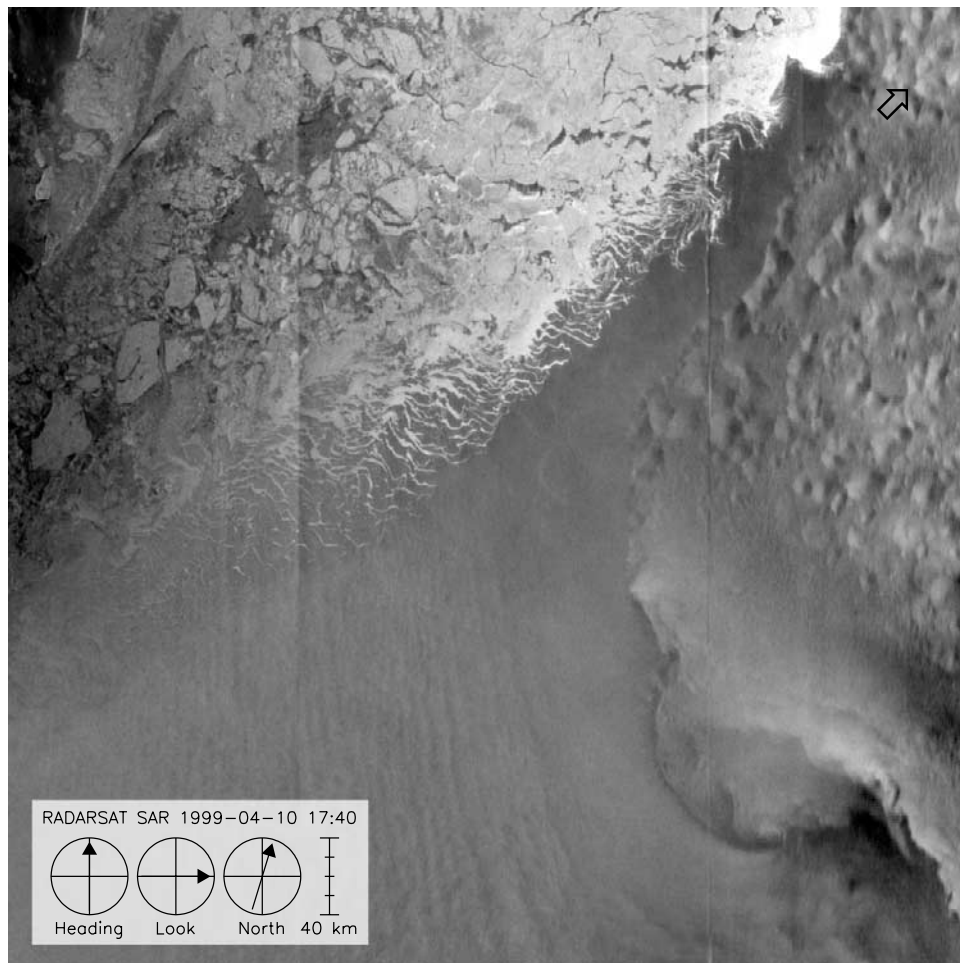
RADARSAT SAR 1999−04−10 17:40

Heading   Look   North   40 km

Figure 3. RADARSAT-1 ScanSAR-Wide image of the scenario of Figure 2, 10 April 1999, 1740 UTC. Imaged area = 500 km × 500 km, full resolution = 100 m (pixel size = 50 m × 50 m), 5.3 GHz, HH, incidence angle = 20°−50° (near range/far range). Image intensities have been corrected (empirically) for variation with incidence angle over water. The arrow in the upper right corner indicates the location of the feature shown in Figure 4. © Canadian Space Agency 1997.

and water and air temperatures were −0.9°C and −10.6°C, respectively, indicating an unstable stratification of the marine atmospheric boundary layer (MABL). Under such conditions, small mesoscale image intensity variations, such as the ones which are visible throughout the whole image, can be attributed to inhomogeneities in the wind field. Surface films or ice were not present in the test area.

3. Interpretation of Radar Signatures of Oceanic and Atmospheric Convection Cells

[14] We will now discuss how the convection cell signatures of Figures 2 and 3 can be interpreted qualitatively and quantitatively, and we will show that the fact that the oceanic convective chimney of Figure 5 is not visible in the ERS-2 SAR image of Figure 6 is consistent with model results. We will use two different modeling approaches: A "top-down" approach, in which the observed SAR signatures are inverted into best fit solutions for surface current and/or wind variations (section 3.1), and a "bottom-up" approach, in which we simulate the hydrodynamics of an oceanic convective chimney by a numerical model and

compute theoretical SAR signatures of such features, which can then be evaluated and compared to actually observed SAR signatures (section 3.2).

3.1. Inversion of SAR Signatures Into Surface Current or Wind Variations

[15] As demonstrated in a number of publications [e.g., *Ufermann and Romeiser*, 1999a, 1999b], state-of-the-art SAR imaging models for the ocean have reached a level of perfection which permits a quite accurate and reliable retrieval of surface current and/or wind variations from observed SAR signatures without much additional information from other sources. This is particularly true if multichannel (multipolarization or multifrequency) imagery is available, which can help to resolve possible ambiguities and to further improve the confidence level of the retrieved data products.

[16] The model inversion works such that input current and/or wind fields of the SAR imaging model are optimized until best agreement between observed and simulated SAR signatures is obtained. The current or wind field which leads to the best reproduction of a SAR signature by the imaging
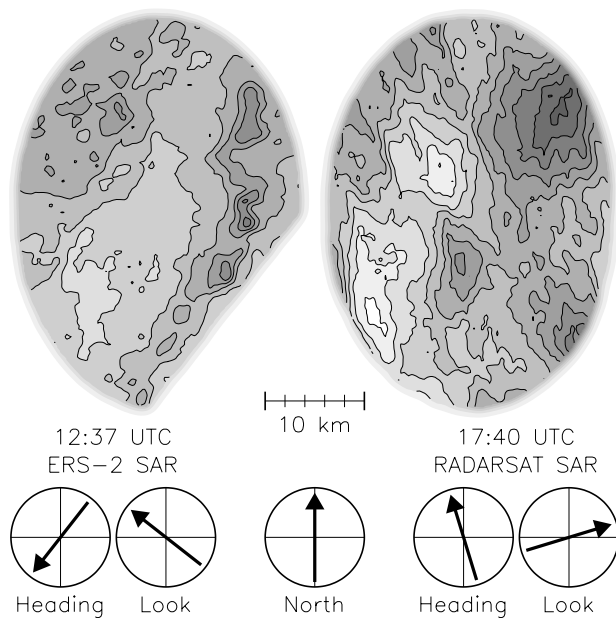
Figure 4. Elliptical subscenes (18 km × 25 km) of (left) the right-hand side of the ERS-2 SAR image of Figure 2 and (right) the upper right corner of the RADARSAT-1 ScanSAR image of Figure 3, showing pronounced signatures of convection cells of about the same size and shape at about the same location. For best visualization, the signatures have been slightly smoothed and normalized by the respective mean values; contour levels are shown with a spacing of 1 dB. Total modulation depths: 5.9 dB and 9.8 dB.
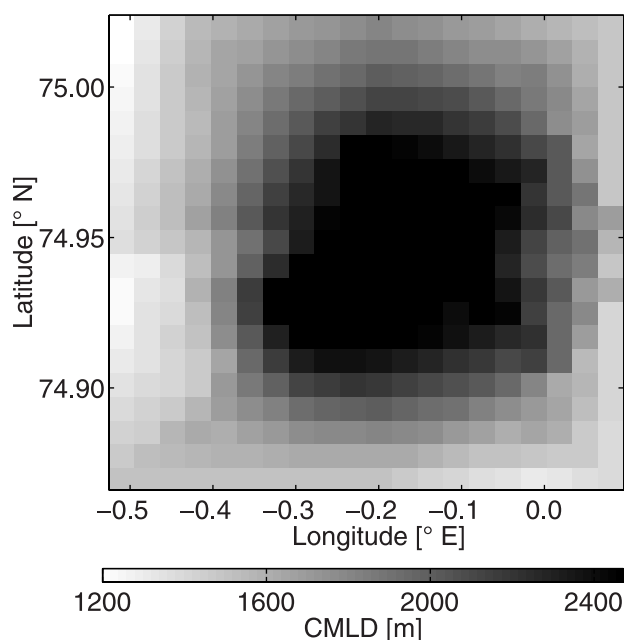
model is then considered as best estimate of the actual current or wind field in the test area. To avoid unrealistic or ambiguous results, and to guide the optimization of the current and wind fields into useful directions, efficient mechanisms for controlling the physical plausibility of all modifications to the input arrays of the SAR imaging model are a crucial element of this method. If possible, one tries to use "feature models" of the expected oceanic or atmospheric features in the test area, which characterize the surface current or wind field by a very limited set of tunable key parameters. Furthermore, specific meteorological conditions such as wind speed and direction as well as near-surface air and sea temperatures in a test area at the time of the SAR image acquisition should be known as accurately as possible.

[17] The oceanic or atmospheric origin of observed SAR signatures is often obvious from their shapes, dimensions, strengths, or locations. In such cases, it is not necessary to try different kinds of feature models. Also, in the case of Figures 2 and 3, experienced users of SAR imagery may say immediately that the observed signatures look very much like typical signatures of atmospheric convection cells, and thus this should be the most likely interpretation. However, we will show in the following that wind variations are in fact the only possible explanation for the observed ERS-2 and RADARSAT-1 SAR signatures. We can come to this conclusion without a priori assumptions regarding the oceanic or atmospheric nature of the observed phenomenon.

3.1.1. Numerical Modeling of SAR Signatures of Spatially Varying Surface Current and Wind Fields

[18] The numerical model used for our simulations is the SAR imaging model M4S of the University of Hamburg [*Romeiser et al.*, 1997; *Romeiser and Alpers*, 1997], which

Figure 5. Convective mixed layer depth (CMLD) at a test site in the Greenland Sea on 26 February 2002, as obtained from in situ measurements from RV *Lance*. Total area size is ~17 km × 17 km.
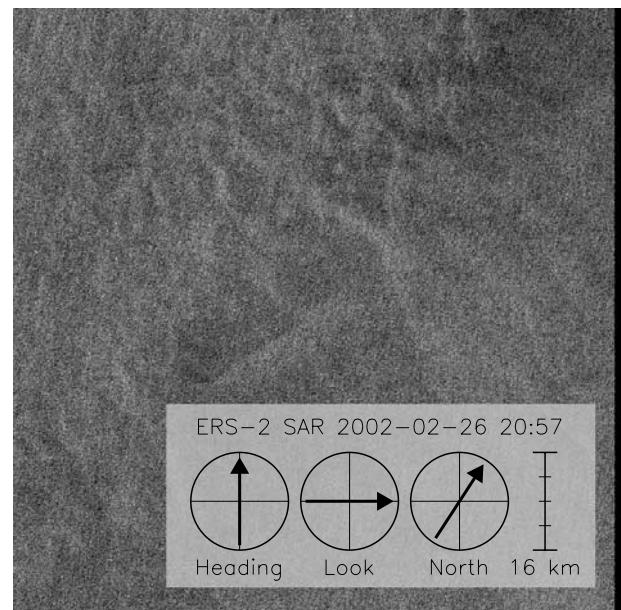

Figure 6. ERS-2 SAR image of a scenario in the Greenland Sea which includes (near the center of the left-hand border) the area of well-known oceanic convection depicted in Figure 5; 26 February 2002, 2057 UTC. Radar and image parameters are the same as in Figure 2. © ESA 2002.
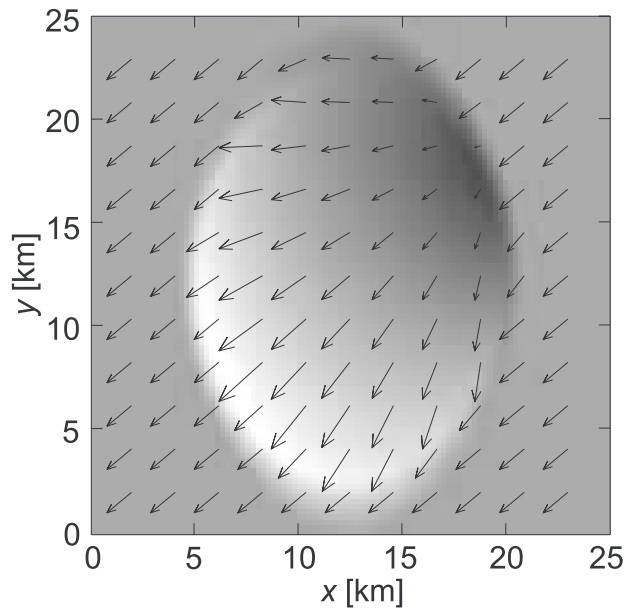
Figure 7. Schematic plot of an idealized surface wind field of an "open" atmospheric convection cell with a superimposed ambient wind from the upper right corner. Shading levels indicate magnitude of wind speed. Wind fields and current fields of this kind, with an actual grid resolution of 250 m × 250 m, were used as input fields for our SAR imaging simulations.

can simulate various kinds of radar signatures of spatially varying surface current and wind fields, and which has already been used by us for similar investigations on SAR signatures of oceanic and atmospheric features at the Gulf Stream front [*Ufermann and Romeiser*, 1999a, 1999b] and for several other studies. The M4S model suite consists of a composite surface scattering model for the simulation of backscattered radar signals from the ocean and the formation of SAR imagery, including specific artifacts of the SAR imaging mechanism, and a wave-current-wind interaction model for the simulation of the modulation of the ocean wave spectrum by spatially varying surface current and wind fields.

[19] Recent improvements of M4S include the addition of terms which account for contributions of specular reflection to the radar return from the ocean surface. These contributions can become large at steep incidence angles below about 30°. They are thus quite important for the simulation of ERS SAR signatures (nominal incidence angle = 23°). Furthermore, SAR images with realistic statistical properties can be simulated: The standard output of M4S is an expectation-value SAR image which corresponds to an ensemble average of an infinite number of realizations of actual SAR images. The expectation-value SAR image does not exhibit the characteristic statistical image intensity fluctuations in actual SAR images, which are known as "speckle noise" and which result from fundamental principles of coherent radar backscatter measurements [*Ulaby et al.*, 1986]. To get an impression of the visibility of simulated (weak) SAR signatures in actual imagery, M4S can generate realizations of images with the χ^2 distribution of pixel intensity values which corresponds to the given

number of independent samples (looks) per pixel. Standard images from ERS-2 SAR and RADARSAT-1 ScanSAR are processed with three looks and four to eight looks (near range/far range) at the original pixel sizes of 12.5 m × 12.5 m and 50.0 m × 50.0 m, respectively. The effective number of independent looks at a given reduced resolution is equal to the number of looks of the original image multiplied by the ratio between the new pixel size and the original pixel size.

[20] As discussed in the paper by *Ufermann and Romeiser* [1999a], the only wind parameter in M4S is the wind speed at a height of 10 m for a neutrally stratified atmosphere; the friction velocity or other parameters determined by the atmospheric stratification cannot be adjusted separately. Instead, all wind stress variations to be considered in M4S simulations must be translated into equivalent wind speed variations at a height of 10 m in a neutrally stratified atmosphere.

3.1.2. Feature Models for Oceanic and Atmospheric Convection Cells

[21] Following *Mitnik* [1992] and *Ufermann and Romeiser* [1999b], we parameterize the near-surface wind field of a circular "open" atmospheric convection cell (i.e., a convection cell with a divergent horizontal flow pattern at the surface) by a radial wind from the center to the outside of the cell. The magnitude of the wind is proportional to the distance from the cell's center within the inner 5/6 of the radius of the cell and falls back to 0 within the outer 1/6 of the radius. To obtain an elliptic convection cell corresponding to the observed radar signatures, we deform the circular flow pattern accordingly. A constant ambient wind vector can be superimposed by simple addition. Figure 7 shows an example of an idealized wind field of an atmospheric convection cell generated this way. Parameters to be optimized in the SAR image simulations are the maximum cell-induced wind and, to some extent, the ambient wind.

[22] For the simulation of oceanic features, we assume that current variations of the observed spatial dimensions must result from a large rotating, vortex-like water body, which could be a convective chimney or, in principle, a rotating water lens of reduced density which is floating on the ambient water. On the basis of our feature model for atmospheric convection cells, we assume that the magnitude of the surface current grows linearly from 0 in the center to a given maximum value (say, 0.1 m/s) at 5/6 of the total radius and falls back to 0 within the remaining 1/6. Owing to the variety of possible physical explanations, the orientation of the rotation is not obvious from the beginning; thus we try both cyclonic and anti-cyclonic model current fields.

3.1.3. Retrieval of Ambient Wind Vectors and Other Meteorological Parameters

[23] An important fundamental parameter for the SAR signature inversion is the mean (or ambient) wind vector, which determines the mean NRCS of the image and the strength of radar signatures of spatial variations in the surface wind and current fields. In principle, one can determine the wind speed and direction from a SAR image itself [*Horstmann et al.*, 2000; *Monaldo et al.*, 2001], but a fully functional algorithm for doing this is not available to us. For the interpretation of the convection cell signatures in the SAR images of Figures 2 and 3, we use a weather chart
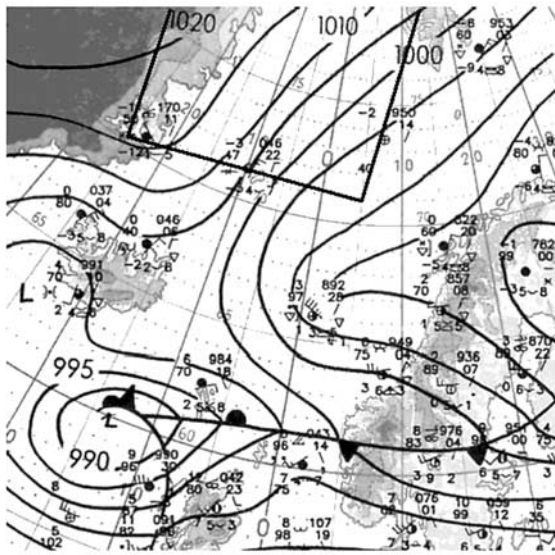
Figure 8. Surface weather chart of the Greenland Sea for 10 April 1999, 0000 UTC. The black frame indicates the coverage of the map of Figure 1. Reproduced with permission of Deutscher Wetterdienst, Offenbach, Germany, 1999.

from the German National Meteorological Service to determine the wind direction and an empirical wind scatterometer model to determine the wind speed from the mean SAR image intensity in the region of interest. For the scenario of Figure 6, the wind speed is known from in situ measurements (see section 2.2).

[24] The surface weather chart of the Greenland Sea for 10 April 1999, 0000 UTC is shown in Figure 8. Between a high-pressure system located over Greenland and an extended low-pressure system over northern Finland, the Greenland Sea was influenced by a cold north to northeasterly airflow. The closest available in situ measurement of atmospheric parameters was taken at Jan Mayen, at ~71.2°N, 8.0°W. These data show a northeasterly wind at

speeds of 10–15 knots (5.0–7.5 m/s), partial cloud coverage, and light snow at an air temperature of −3°C. However, our region of interest is located approximately 700 km northeast of Jan Mayen, i.e., upstream relative to the airflow. It can be expected that the air mass arriving at Jan Mayen has gained a considerable amount of heat on its way between our region of interest and Jan Mayen. Assuming a typical air temperature at the ice edge in the Fram Strait of −20°C and a typical value for the heat transfer into the atmosphere, for example, 200 W/m^2, we estimate the air temperature in the region of interest to be about −12°C. Wind speed and direction are probably very similar at both locations due to the extent of the pressure systems.

[25] Despite the spatial and temporal offset of the meteorological data from the scenario imaged by ERS-2 and RADARSAT-1, they provide a good overview of the meteorological conditions. In addition to the wind information, the fact that there was probably no strong precipitation in the test area is quite valuable for the SAR image interpretation. In principle, heavy rainfall can occur in combination with atmospheric convection cells and can influence the radar signal [*Melsheimer et al.*, 1998]. For the scenario studied here, we can exclude this effect. But the estimated air-sea temperature difference of 10°C in the test area indicates that quite vigorous atmospheric convection could have taken place.

[26] Using the wind direction of about 50° from the weather chart, we can derive the magnitude of the wind vector from the absolute NRCS values of the ERS-2 SAR image, using the well-established empirical ERS wind scatterometer model CMOD4 [*Stoffelen and Anderson*, 1993]. CMOD4 allows a calculation of the NRCS for C band, VV polarization for a given wind speed and viewing geometry (incidence angle and look direction with respect to the wind direction) of the SAR sensor. Doing this for different homogeneous areas of 10 km × 10 km (800 × 800 pixels) around the main region of interest, we obtain good agreement between observed and CMOD4-derived NRCS values for wind speeds of about 4–5 m/s. This is consistent with the surface weather chart. Accordingly, we

Table 1. Wind and Current Scenarios Considered in the Simulations of the Convection Cell SAR Signatures of Figure 4 and Resulting Modulation Depths of the NRCS[a]

Mean Wind, m/s	Wind Variation, m/s	Current Variation, m/s	Modulation Depths, dB			Figure Number
			ERS	RADARSAT	Ratio	
Observed Signatures						
n/a	n/a	n/a	5.9	9.8	3.8	4
Simulated Signatures						
4.5	0.0[a]	0.1C[b]	0.6	0.4	−0.2	
4.5	0.0[a]	0.1A[b]	0.6	0.4	−0.2	
4.5	0.0[a]	0.5C[b]	2.8	2.0	−0.8	9
4.5	0.0[a]	0.5A[b]	2.7	2.1	−0.7	
4.5	0.0[c]	0.5C[b]	2.5	0.6	−1.9	
4.5	0.0[c]	0.5A[b]	2.0	0.7	−1.4	
4.5	2.5	0.0	6.7	8.7	2.0	10
4.5	2.0	0.0	5.2	6.6	1.4	
4.5	3.0	0.0	8.4	11.2	2.8	
4.0	2.5	0.0	7.6	10.3	2.7	
5.0	2.5	0.0	5.9	7.6	1.7	

[a]Local effective wind corrected for local surface current.
[b]C, cyclonic rotation; A, anticyclonic rotation.
[c]Local effective wind not corrected for local surface current.
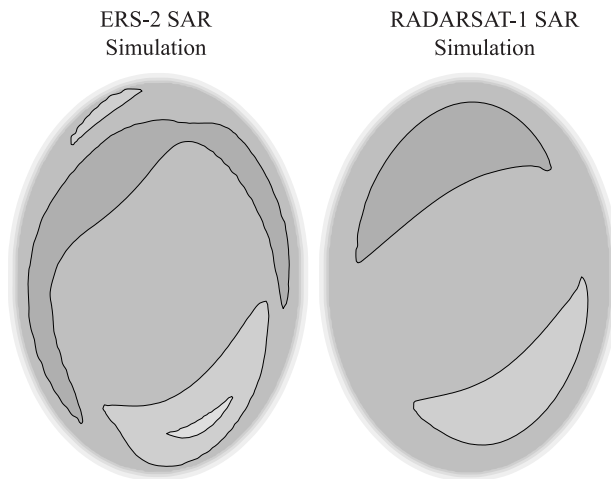
ERS-2 SAR
Simulation

RADARSAT-1 SAR
Simulation

Figure 9. Simulated (left) ERS-2 and (right) RADAR-SAT-1 SAR signatures of the spatially varying current field of a cyclonically rotating water body with a maximum surface current of 0.5 m/s and no ambient current; wind speed = 4.5 m/s from 50°. Contour levels correspond to the ones of Figure 4. Total modulation depths: 2.8 dB and 2.0 dB.

use a nominal (ambient) wind of 4.5 m/s from 50° with respect to north for the M4S model simulations.

3.1.4. Oceanic Convection Cell Simulations

[27] Realistic surface currents of convective chimneys in the Greenland Sea should be on the order of $0.05-0.10$ m/s or less (see section 3.2). If we assume a relatively strong maximum current of 0.10 m/s in our feature model (resulting in a maximum current shear of about 1.3×10^{-5} s^{-1}), the resulting simulated SAR signatures are extremely weak: As listed in Table 1, we obtain modulation depths of only 0.6 dB for the ERS case and 0.4 dB for the RADARSAT case, independent of the orientation of the rotation of the water body (only the shapes of the SAR signatures change with the orientation). These values are much lower than the observed ones. Furthermore, the simulated ERS signatures are found to be stronger than the simulated RADARSAT signatures, while the actual data exhibit a stronger modulation depth in the RADARSAT image.

[28] Figure 9 shows results of additional simulation runs, in which the maximum currents were further increased to 0.50 m/s. Even with such very strong surface currents, the theoretical modulation depths are smaller than the observed ones by several decibels, and the simulated ERS signatures are again stronger than the simulated RADARSAT signatures. Aside from these quantitative shortcomings, the shapes of the simulated SAR signatures look quite different from the observed ones of Figure 4.

[29] In standard setup, local wind vectors in the M4S model are corrected for the local surface current in order to obtain an "effective" wind vector acting on the moving water surface (for example, a nominal wind of 5 m/s over a surface current of 1 m/s will result in an effective wind of $4-6$ m/s, depending on the relative direction between the two vectors). Owing to this effect, the simulated SAR signatures of spatially varying current fields include contributions which result from the effective wind variations

and are physically equivalent to radar signatures of a spatially varying wind field over a water body at rest. To examine the magnitude of these contributions, we have repeated the simulation runs of Figure 9 with the effective wind correction switched off. The resulting modulation depths are listed in Table 1: While the simulated ERS SAR signatures are not affected very much by the wind correction, the simulated RADARSAT modulation depths change from 2.0 to 0.6 dB and from 2.1 to 0.7 dB if the wind correction is switched off, indicating that the simulated RADARSAT ScanSAR signatures of Figure 9 result dominantly from spatial variations in the effective wind vector, not from direct wave-current interaction.

[30] In summary, the results of our SAR imaging simulations suggest that the observed strong convection cell signatures in Figures 2 and 3 cannot result from the presence of oceanic convection features in the test area. Neither the shapes of the observed ERS-2 and RADARSAT-1 SAR signatures, nor their modulation depths or their characteristic differences (stronger modulation in the RADARSAT image) are consistent with theoretical properties of SAR signatures of oceanic convection cells.

3.1.5. Atmospheric Convection Cell Simulations

[31] We have performed a number of simulation runs with wind fields of atmospheric convection cells, using different combinations of maximum convection-induced wind speeds and ambient wind speeds. Both parameters were changed in steps of 0.5 m/s. The best result with the nominal ambient wind of 4.5 m/s from 50° is shown in Figure 10: Using a maximum convection-induced wind of 2.5 m/s, which appears to be a reasonable value (again, this is not necessarily the actual variation of the wind speed at a height of 10 m but just a wind variation equivalent to the effect of the actual wind stress variations), we obtain reasonable shapes of the simulated signatures and modulation depths of 6.7 dB for the
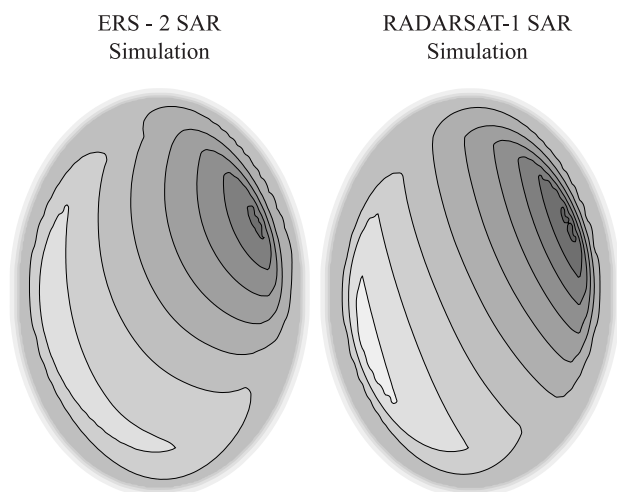
ERS - 2 SAR
Simulation

RADARSAT-1 SAR
Simulation

Figure 10. Simulated (left) ERS-2 and (right) RADARSAT-1 SAR signatures of the spatially varying wind field of an atmospheric convection cell with divergent surface flow ("open cell"), effective wind variations by ±2.5 m/s and an ambient wind of 4.5 m/s from 50°. Contour levels correspond to the ones of Figure 4. Total modulation depths: 6.7 dB and 8.7 dB.
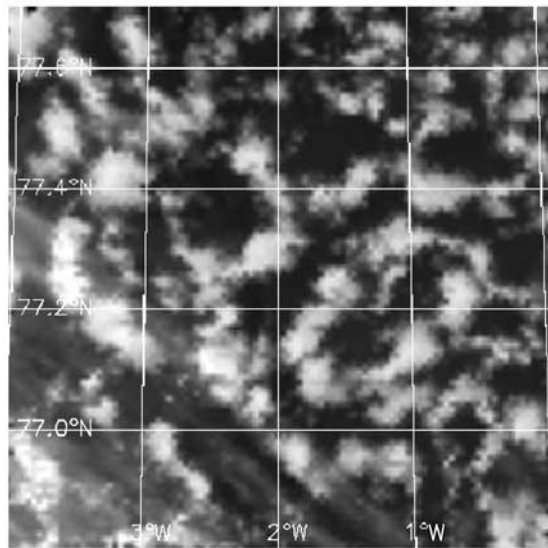
Figure 11. Subscene (100 km × 100 km) of an infrared image (NOAA AVHRR, channel 4) of the Greenland Sea test area, 10 April 1999, 1705 UTC. © National Oceanic and Atmospheric Administration (from NOAA Satellite Active Archive, http://www.saa.noaa.gov).

ERS SAR parameters and 8.7 dB for the RADARSAT ScanSAR parameters, i.e., deviations of +0.8 dB and −1.1 dB, respectively, from the observed modulation depths. This indicates much better agreement than in the current field simulations discussed in the previous subsection. Again, all wind and current scenarios considered in the simulation runs and the resulting modulation depths are summarized in Table 1.

[32] Differences on the order of 1 dB between observed and simulated modulation depths may result from remaining model shortcomings or from changes of the environmental conditions during the 5 hours between the ERS-2 and RADARSAT-1 overpasses. According to Table 1, modifications of the wind variations and the ambient wind speed by 0.5 m/s result in changes of the simulated modulation depths by about 2 dB and 1 dB, respectively; thus the SAR signatures are quite sensitive to relatively small changes in the wind field.

[33] Given the simple parameterization of wind stress variations in terms of equivalent wind speed variations at a height of 10 m, and given the fact that the M4S model has not been specifically optimized for wind stress retrieval, it is difficult to relate the best fit wind variations obtained from our model simulations to actual physical parameters of atmospheric convection cells. However, our results indicate very clearly that the observed SAR signatures can be explained as signatures of atmospheric convection cells and not as signatures of oceanic ones. It should be possible to retrieve quantitative information on wind stress variations and on the three-dimensional atmospheric flow from the SAR signatures by using more specific MABL/air-sea interaction models. The sensitivity of the simulated SAR signatures to changes in the convection-induced wind variations and in the ambient wind vector is

high. Thus great accuracy could be expected from a model-based algorithm for the retrieval of wind stress variations from SAR signatures. For other examples of analyses of radar signatures of atmospheric convection features, see the papers by *Mitnik* [1992], *Alpers and Brümmer* [1994], and *Sikora and Thompson* [2002]. A comprehensive review of experimental and theoretical findings on the physics and characteristic properties of atmospheric convection cells was given by *Atkinson and Zhang* [1996].

[34] Finally, independent data from another source show that our interpretation of the observed SAR signatures is, at least qualitatively, correct: The dashed square in Figure 1 shows the location of a 100 km × 100 km subscene of a NOAA AVHRR infrared image (channel 4) which was acquired 35 min prior to the acquisition of the RADARSAT image of Figure 3. This AVHRR subscene is shown in Figure 11. It exhibits bright (i.e., cold) signatures of clouds over the entire subscene. The characteristic shape and the dimensions of the cloud pattern are commonly associated with "open" convection cells in which clouds formed in the MABL align in a hexagonal structure. Such cells form at low to moderate surface wind speeds. The clouds may generate some precipitation which, however, can be expected to be light to moderate snow in this low-temperature environment. It should not have a visible effect on SAR signatures.

3.2. Forward Simulation of Surface Current Fields and SAR Signatures of Oceanic Convection Features

[35] Inspired by the results of *Fischer et al.* [1999], we have implemented a numerical model for oceanic deep convection in the Greenland Sea to study such features in detail and to obtain the best possible surface current fields for computing SAR signatures. Some key model characteristics and results will be discussed in the following.

3.2.1. Numerical Modeling of Oceanic Convection Features

[36] The formation of oceanic convection cells due to local cooling at the surface can be simulated by a numerical hydrostatic/nonhydrostatic convection model, following the approach of *Mahadevan et al.* [1996], *Androsov et al.* [2001], *Romanenkov et al.* [2001], and *Androsov et al.* [2002]. The model implemented at the University of Hamburg, which is called GNOM (General Nonhydrostatic Ocean Model), is a high-resolution, nonlinear, three-dimensional hydrostatic/nonhydrostatic model. It is based on a three-dimensional boundary value problem for the momentum, continuity, density-constituents, and turbulence-characteristics equations. The model is implemented in boundary-fitted curvilinear coordinates and vertical σ coordinates to simulate the mesoscale circulation in an ocean basin characterized by large convective activity. The numerical method is based on composition schemes for split operators, with particular attention to advection representation and vertical structure of the solution. The horizontal grid for the Greenland Sea test area has about 200 × 200 or 400 × 400 nodes with a horizontal spacing of 125 m or 62.5 m, respectively. In the vertical, 40 levels are used.

[37] The initialization of the model is performed from a condition of rest. Two different initial scenarios are used: Simulations of plume-scale features start with an initial
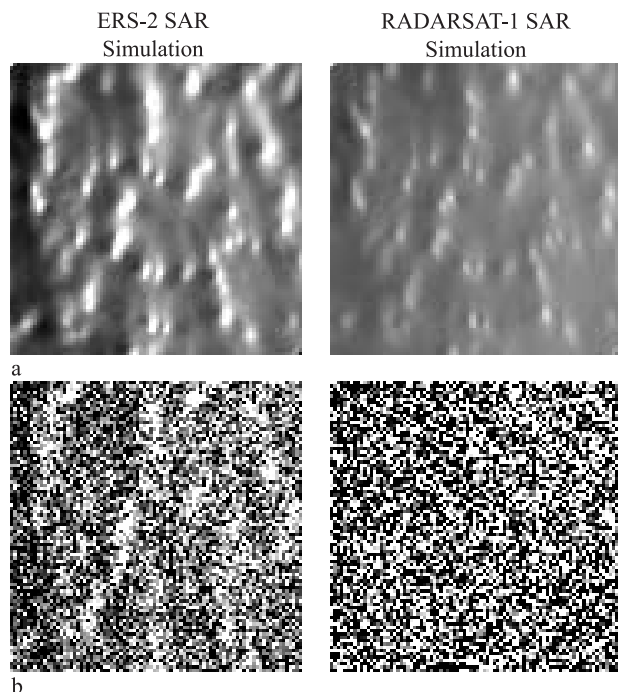
ERS-2 SAR
Simulation

RADARSAT-1 SAR
Simulation

a

b

Figure 12. Examples of simulated (left) ERS-2 and (right) RADARSAT-1 SAR signatures of the surface current field of oceanic convection plumes from the GNOM model, resembling results of *Fischer et al.* [1999]. (a) Expectation value images. (b) Realizations with realistic speckle noise statistics. ERS-2 SAR and RADARSAT-1 ScanSAR parameters correspond to the scenarios of Figures 2 and 3, respectively. Test area size is 5.5 km × 5.5 km, model grid resolution (and pixel size of the simulated images) is 62.5 m × 62.5 m, intensity range from black to white is 1.0 dB.

homogeneous ocean; the plume features are solely generated as a result of local cooling by the wind. For the simulation of larger eddy features, we prescribe a two-layer density field as initial field. The interface between the two layers is at a depth of 250 m. In the central part of the test area, with a diameter of about 12 km, deep-water water mass characteristics are used throughout the whole water column, representing an idealized preconditioning of deep-water convection. The total convection layer depth is 2000 m. In addition to the density differences, the net heat flux at the water surface and the wind speed are input parameters of a simulation run. During the spin-up time of 1 day, a constant initial pressure gradient without external forces is used, except for the Coriolis force.

[38] As in the simulations of section 3.1, the surface current fields obtained from GNOM are used as input current fields for the M4S model to obtain simulated SAR signatures and to evaluate the visibility of these signatures in an actual SAR image from ERS-1/ERS-2, RADARSAT-1, and other existing and upcoming remote sensing satellites.

3.2.2. Small-Scale Convection Plume Simulations

[39] To check the consistency of our models with the ones used by *Fischer et al.* [1999], we have performed a simulation run for a scenario similar to that of their Figure 5. Using an initial water temperature of 3.02°C (homogeneous initial conditions), a net surface heat flux

of 400 W/m^2, and a wind of 3.5 m/s from north, we obtain a number of convective plumes with diameters on the order of 1 km in the center of the chimney. The maximum surface current velocity is about 0.12 m/s. Simulated ERS-2 and RADARSAT-1 SAR images of this scenario, using radar parameters and the imaging geometries of Figures 2 and 3, respectively, are shown in Figure 12.

[40] The two upper images (Figure 12a) show expectation value SAR images, corresponding to the model results shown in Figures 9 and 10. As expected, the simulated ERS-2 and RADARSAT-1 SAR signatures of the given scenario are quite similar (in terms of shapes, dimensions, and modulation depths) to the ones obtained by *Fischer et al.* [1999]. A look at our simulated images with speckle noise (Figure 12b), which have been generated in addition to the expectation-value images, reveals that the signatures would be much less pronounced in actual SAR images with realistic noise statistics. Only the simulated ERS-2 image with speckle noise exhibits signatures of the convection feature which should be clearly visible.

[41] An actual ERS-2 SAR image with signatures similar to the ones predicted by *Fischer et al.* [1999] was presented and discussed by *Mitnik et al.* [2000]. The signatures were observed in the Japan Sea, south of Vladivostok, on 21 January 1998. Oceanic deep convection is likely to occur in this region and at this time of the year. However, the actual origin of the SAR signatures of interest is not clear.
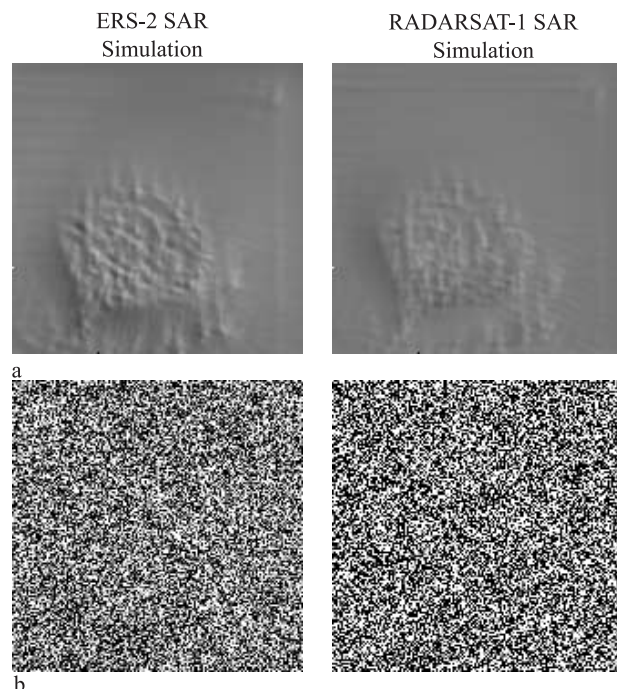
ERS-2 SAR
Simulation

RADARSAT-1 SAR
Simulation

a

b

Figure 13. Same as Figure 12, but simulating the scenario encountered during the RV *Lance* cruise (Figure 5) and observed by ERS-2 (Figure 6). ERS-2 and RADARSAT-1 ScanSAR parameters correspond to the scenarios of Figures 6 and 3, respectively (an actual RADARSAT ScanSAR image of this scenario is not available to us). Test area size is 20 km × 20 km; model grid resolution is 125 m × 125 m, intensity range is 0.4 dB.

ERS-2 SAR
Simulation

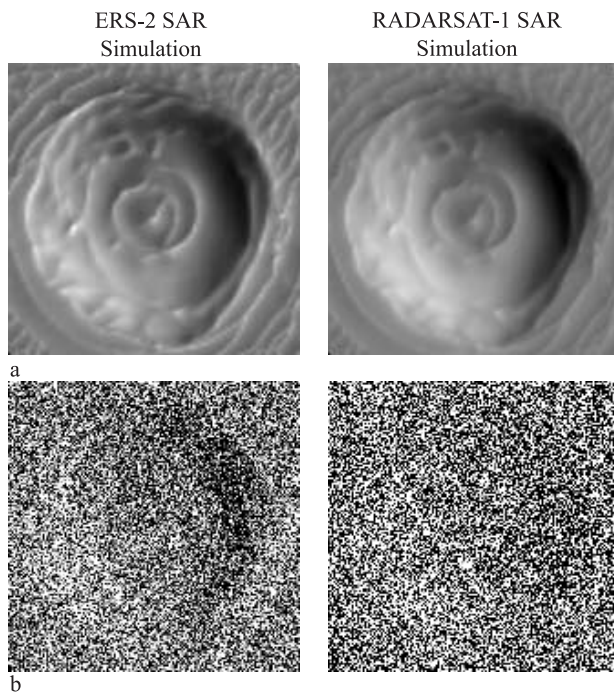RADARSAT-1 SAR
Simulation

Figure 14. Same as Figure 13, but for an idealized strong convection chimney from the GNOM model (see text).

Other signatures in the same image can clearly be attributed to the presence of atmospheric convection cells.

3.2.3. Simulations for the Scenario of Figures 5 and 6

[42] Another simulation run has been performed for the oceanic convection scenario of Figure 5, based on the in situ observations carried out aboard RV *Lance*. In this case, the water temperatures are $T_{ambient} = -0.84°C$ and $T_{chimney} = -0.98°C$ (preconditioned two-layer initial scenario), the net surface heat flux is 190 W/m^2, and the wind is 15 m/s from 330°. Again, we obtain many individual small convective plumes, which are forced to a mean southward motion by the strong wind. The maximum surface current after a simulation period of 1 day for initialization and two additional days is on the order of 0.15 m/s. SAR simulations were performed for ERS-2 parameters corresponding to the actual ERS-2 SAR image of this scenario shown in Figure 6 and, for compatibility with other model results, for RADARSAT-1 ScanSAR parameters from the scenario of Figure 3. The simulated images are shown in Figure 13.

[43] Owing to the high wind speed and the resulting small intensity variations of surface waves due to hydrodynamic wave-current interaction, the simulated SAR signatures for this case are clearly less pronounced than the ones discussed in the previous subsection. Such weak signatures would not be detectable in an actual SAR image. Accordingly, there is no contradiction between the presence of a strong convection feature according to the in situ data and a complete absence of signatures of this feature in the ERS-2 SAR image of Figure 6.

3.2.4. Simulations for an Idealized Strong Convection Scenario

[44] To find out whether oceanic convection features in the Greenland Sea can become visible in SAR imagery at all, another simulation run has been performed for a scenario resulting in particularly strong convection and relatively strong surface current gradients with a moderate wind speed at the time of the SAR image acquisition. This scenario is characterized by $T_{ambient} = -0.84°C$, $T_{chimney} = -1.02°C$, a net surface heat flux of 215 W/m^2, and a wind of 9 m/s from 330° for the first 2 days, followed by 2 m/s from 330° for another 3 days, after which the simulated SAR images were generated. They are shown in Figure 14. The maximum surface current in this case is 0.06 m/s.

[45] The oceanic and atmospheric conditions in this particular case lead to the formation of a large rotating convective chimney as a whole instead of the small convection cells (plumes) obtained in the previous examples. At the low wind speed of 2 m/s, which is favorable for strong wave-current interaction, this large rotating water body becomes faintly visible in the simulated ERS-2 SAR image (Figure 14a). The main reason for the better visibility of the chimney in the ERS-2 image, compared to the RADARSAT-1 image (Figure 14b), is the higher spatial resolution (smaller pixel size) of ERS-2, which permits to average over a larger number of independent looks within one model grid cell of 125 m × 125 m (about 300 looks for ERS-2 and 50 looks for RADARSAT-1; see section 3.1.1).

[46] However, even the faintly visible signatures of convective chimneys in the simulated ERS-2 SAR image would not be easily detectable in an actual image. They could be camouflaged by superimposed signatures of other phenomena, and an accurate quantitative interpretation would be practically impossible. In summary, we must conclude from our model results that it is quite unlikely to observe signatures of oceanic convection in the Greenland Sea in ERS-2 or RADARSAT-1 SAR imagery, since most convection features will be too weak to give rise to a sufficiently strong modulation of the NRCS. Only very strong convection events may cause clear SAR signatures under favorable conditions. Accordingly, the fact that signatures of oceanic convection features are not visible in a particular SAR image does not indicate that such features are not present; existing SAR sensors are just not sufficiently sensitive to detect all of them.

3.2.5. Analysis of Future Spaceborne SAR Capabilities

[47] Speckle noise in SAR imagery can be reduced by averaging over many pixels. Upcoming high-resolution SAR systems will offer much smaller pixel sizes than ERS-2 and RADARSAT-1, which correspond to larger numbers of independent looks and thus less speckle noise at a given spatial resolution. Furthermore, dual-polarization SAR systems permit a simultaneous acquisition of images at VV and HH polarization. Theoretically, this can be very useful for the distinction between SAR signatures of oceanic and atmospheric phenomena [*Ufermann and Romeiser*, 1999b]. To evaluate the effect of these improvements on the detectability of oceanic convection features, we have performed some simulations of data products of new and upcoming spaceborne SAR systems.

[48] Dual polarization modes have been implemented with the Advanced SAR (ASAR) of the European remote sensing satellite ENVISAT [*Attema et al.*, 1998], which was launched on 1 March 2002, as well as with the SAR on the upcoming Canadian satellite RADARSAT-2 [*Canadian Space Agency*, 2000], to be launched in 2004. Unfortunately,

TerraSAR-X (VV)
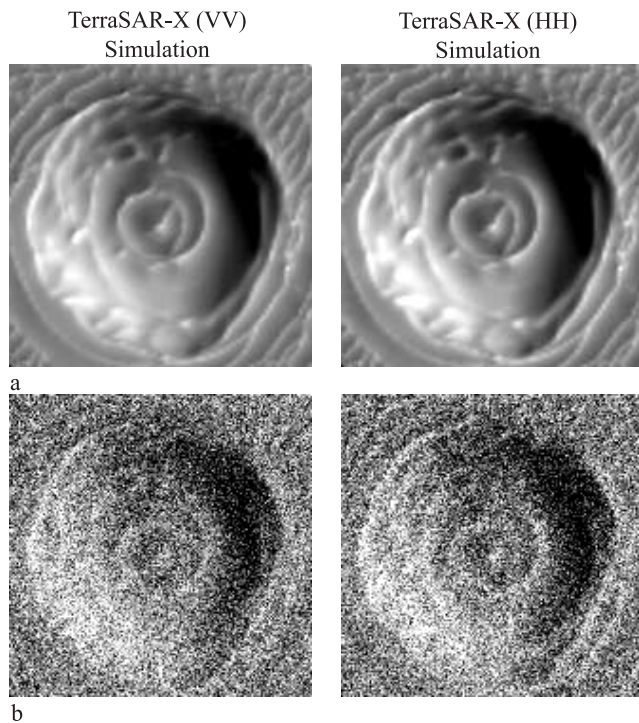Simulation

TerraSAR-X (HH)
Simulation

a

b

Figure 15. Same as Figure 14, but simulating high-resolution TerraSAR-X Stripmap Mode imagery at (left) VV and (right) HH polarization, X band (9.6 GHz), incidence angle is 23°, with the flight and look directions of ERS-2 SAR in the case of Figure 2.

the image quality (in terms of spatial resolution and number of independent looks) of the dual polarization mode data from these sensors will not be better than the quality of ERS-2 imagery; thus the visibility of oceanic convection features in the Greenland Sea will not be better either.

[49] High-resolution imaging capabilities with one single (selectable) polarization and limited swath widths will be available from RADARSAT-2 as well as from the upcoming German satellite TerraSAR-X, which will be launched in 2005 [*Suess et al.*, 2002]. In the case of TerraSAR-X, which will use X band (9.6 GHz), the single-look resolution can be as high as 3 m × 3 m with a swath width of 30 km and a selectable incidence angle between 15° and 60° (full performance between 20° and 45°) [*Suess et al.*, 2002]. Unfortunately, the instrument noise of the TerraSAR-X system is relatively high (noise-equivalent NRCS = −19 dB), which can be a serious problem for measurements over water at high incidence angles and low wind speeds. However, the NRCS of the ocean at X band and incidence angles between 20° and 25° should be sufficiently large for practically all applications.

[50] Simulation results for TerraSAR-X are shown in Figure 15. The scenario is identical to the one of the ERS-2 simulation of Figure 14, except for the different radar frequency and the number of looks of 1736 per grid cell (ERS-2 SAR: 300; RADARSAT-1 ScanSAR: 50). Instead of an ERS-2 image and a RADARSAT-1 image, we have now simulated TerraSAR-X images for the viewing geometry of ERS-2 in Figure 6 (and in Figure 14) and for VV and HH polarization. The simulated images of

Figure 15b with speckle noise account for the expected instrument noise of TerraSAR-X of −19 dB.

[51] In this case, the SAR signatures of the convective chimney become visible quite clearly. One can imagine that even for less favorable conditions, the chances to observe convective chimneys in the Greenland Sea with TerraSAR-X are reasonable, although problems with strong SAR signatures of other phenomena, which may dominate the images and camouflage the weak signatures of oceanic convection features, will persist. The distinction between SAR signatures of oceanic and atmospheric origin in dual-polarization imagery (if such data are available) will not work too well if the signatures are very weak: As discussed at the end of section 3.1.4, SAR signatures of small surface current variations are often dominated by effects of the spatially varying effective wind experienced by the moving water surface. Characteristic polarization-dependent differences between radar signatures resulting from hydrodynamic modulation and from wind variations will have a very small effect under such conditions, and the exploitation of such differences for a distinction between signatures of oceanic and atmospheric phenomena, as proposed by *Ufermann and Romeiser* [1999b], may be not feasible.

4. Conclusions

[52] We have shown and analyzed some examples of SAR images of convection features in the Greenland Sea. The strong mottled signatures in the first example could clearly be attributed to the presence of atmospheric convection cells: Our SAR imaging model results indicate that only wind variations over the ocean in the test area can generate C band SAR signatures of the observed strength (modulation depths of several dB) and with the observed quantitative differences between the ERS-2 SAR image (VV polarization, steep incidence angle, looking toward northwest) and the RADARSAT-1 ScanSAR image (HH polarization, higher incidence angle, looking toward east-northeast). Available additional information from a weather chart and a NOAA AVHRR infrared image confirms the presence of atmospheric convection cells in the test area at the time of the SAR image acquisition. In principle, one can obtain quantitative information on the mean wind, the wind variations in the atmospheric convection cells, and corresponding parameters describing the atmospheric stratification from the SAR signatures themselves, without any additional data from other sources [*Horstmann et al.*, 2000; *Monaldo et al.*, 2001; *Sikora and Thompson*, 2002].

[53] Our second example has been a scenario with a known convective chimney (from in situ measurements) within the area covered by an ERS-2 SAR image which does not exhibit any visible signatures of this feature. Our SAR simulation results with current fields from the numerical oceanic convection model GNOM indicate that the surface current gradients in this case were not sufficiently strong to give rise to a sufficient modulation of the sea surface roughness to become visible in the ERS-2 SAR image.

[54] Further simulation results indicate that it will be generally difficult to observe signatures of oceanic convection features in the Greenland Sea with existing spaceborne SAR systems, since such signatures will usually be quite

weak compared to the inherent speckle noise dynamics of the SAR images (assuming that the water surface is not covered with surface films or ice, which could act as tracers for the visualization of streamlines). Only strong convection events may give rise to significant SAR signatures under favorable conditions. This situation will improve with the availability of high-resolution SAR imagery from space-borne SAR systems such as the ones on the Canadian RADARSAT-2 (to be launched in 2004) and the German TerraSAR-X (to be launched in 2005). The high nominal resolution of these SAR systems on the order of 3 m permits averaging over a large number of independent samples to obtain a significant noise reduction at resulting resolutions comparable to ERS-2 or RADARSAT-1 imagery. NRCS variations of less than 1 dB within a few hundred meters, thus typical SAR signatures of oceanic convection features, will be detectable much more easily with these systems.

[55] In view of an operational monitoring of oceanic convection in the Greenland Sea from space under clean-surface conditions, we conclude from these findings that upcoming spaceborne high-resolution SARs with small pixel sizes and corresponding reduced speckle noise levels will be suited for the detection of some range of oceanic convection features of different strengths, while existing systems such as ERS-2 SAR, RADARSAT-1 SAR, or ENVISAT ASAR are only sensitive to NRCS variations associated with quite strong convection events. The fact that the weak signatures of oceanic convection features in the Greenland Sea have not been found in most SAR images from these existing instruments does not indicate that such features are not present.

[56] The improved monitoring capabilities of high-resolution SARs will permit more frequent observations of oceanic convection features under various oceanic and atmospheric conditions. This can be very valuable for an improved understanding of the complex physics of the important convection phenomena, for model validation or data assimilation purposes, and for statistical analyses. Unfortunately, the weak SAR signatures of oceanic convection features may sometimes be camouflaged by super-imposed signatures of other (atmospheric or oceanic) phenomena, and the distinction between signatures of oceanic and atmospheric phenomena in dual-polarization imagery on the basis of characteristic polarization dependencies will only work if the signatures are sufficiently strong. However, it should usually be possible to identify and distinguish SAR signatures of oceanic or atmospheric convection features on the basis of characteristic shapes, dimensions, and strengths, as well as places, times, and environmental scenarios of their occurrence.

References

Alpers, W., and B. Brümmer (1994), Atmospheric boundary layer rolls observed by the synthetic aperture radar aboard the ERS-1 satellite, *J. Geophys. Res.*, *99*, 12,613–12,621.

Androsov, A., Y. Liberman, D. Romanenkov, and N. Voltzinger (2001), Modelling of a 3-d dynamics and hydrology of the straits: Numerical method/research activities in atmospheric and oceanic modelling, *WMO/TD-1064*, pp. 8.1–8.2, World Meteorol. Org., Geneva.

Androsov, A. A., N. E. Voltzinger, and D. A. Romanenkov (2002), Simulation of three-dimensional baroclinic tidal dynamics in the Strait of Messina, *Izv. Atmos. Oceanic Phys.*, *38*(1), 105–118.

Atkinson, B. W., and J. W. Zhang (1996), Mesoscale shallow convection in the atmosphere, *Rev. Geophys.*, *34*, 403–431.

Attema, E., et al. (1998), Envisat ASAR science and applications, *ESA Publ. SP-1225*, 59 pp., ESA Publ. Div., ESTEC, Noordwijk, Netherlands. (Available at http://earth.esa.int/pub/ESA_DOC/SP_1225.pdf)

Broecker, W. S. (1991), The great ocean conveyer, *Oceanography*, *4*, 79–89.

Canadian Space Agency (2000), RADARSAT-2, A new era in Earth Observation, technical brochure, 4 pp., Saint-Hubert, Québec. (Available at http://www.space.gc.ca/asc/eng/csa_sectors/earth/radarsat2/inf_tech.asp#Publication)

Carsey, F. D., and A. T. Roach (1994), Oceanic convection in the Greenland Sea Odden region as interpreted in satellite data, in *The Polar Oceans and Their Role in Shaping the Global Environment*, Geophys. Monogr. Ser., vol. 85, edited by O. M. Johannessen et al., pp. 211–222, AGU, Washington, D. C.

Fischer, K. W., S. Legg, W. H. Munk, R. A. Shuchman, R. W. Garwood, and J. P. Palshook (1999), Modeled radar surface signature of deep ocean convection, *IEEE Trans. Geosci. Remote Sens.*, *37*(4), 2050–2067.

Horstmann, J., W. Koch, S. Lehner, and R. Tonboe (2000), Wind retrieval over the ocean using synthetic aperture radar with C-band HH polarization, *IEEE Trans. Geosci. Remote Sens.*, *38*, 2122–2131.

Johannessen, O. M., S. Sandven, W. P. Budgell, J. A. Johannessen, and R. A. Shuchman (1994), Observation and simulation of ice tongues and vortex pairs in the marginal ice zone, in *The Polar Oceans and Their Role in Shaping the Global Environment*, Geophys. Monogr. Ser., vol. 85, edited by O. M. Johannessen et al., pp. 109–136, AGU, Washington, D. C.

Mahadevan, A., J. Oliger, and R. Street (1996), A nonhydrostatic mesoscale ocean model: II. Numerical implementation, *J. Phys. Oceanogr.*, *26*, 1868–1880.

Marshall, J., and F. Schott (1999), Open-ocean convection: observations, theory and models, *Rev. Geophys.*, *37*, 1–64.

MEDOC Group (1970), Observations of formation of deep-water in the Mediterranean Sea, 1969, *Nature*, *227*, 1037–1040.

Melsheimer, C., W. Alpers, and M. Gade (1998), Investigation of multi-frequency/multi-polarization radar signatures of rain cells over the ocean using SIR-C/X-SAR data, *J. Geophys. Res.*, *103*, 18,867–18,884.

Mitnik, L. M. (1992), Mesoscale coherent structures in the surface wind field during cold air outbreaks over the far eastern seas from the satellite side looking radar, *La Mer*, *30*, 287–296.

Mitnik, L. M., V. A. Dubina, and V. B. Lobanov (2000), Cold season features of the Japan Sea coastal zone revealed by ERS SAR, in *Proceedings of ERS-Envisat Symposium "Looking Down to Earth in the New Millennium"* [CD-ROM], *ESA CD SP-461*, Eur. Space Agency Publ. Div., Noordwijk, Netherlands.

Monaldo, F. M., D. R. Thompson, R. C. Beal, W. G. Pichel, and P. Clemente-Colon (2001), Comparison of SAR-derived wind speed with model predictions and ocean buoy measurements, *IEEE Trans. Geosci. Remote Sens.*, *39*, 2587–2600.

Morawetz, W. M. L., P. J. Sutton, P. F. Worcester, B. D. Cornuelle, J. F. Lynch, and R. Pawlowicz (1996), Three dimensional observations of a deep convective chimney in the Greenland Sea during winter 1988/89, *J. Phys. Oceanogr.*, *26*, 2316–2343.

Romanenkov, D. A., A. A. Androsov, and N. E. Voltzinger (2001), Comparison of forms of the viscous shallow-water equations in the boundary-fitted coordinates, *Ocean Modelling*, *3*, 193–216.

Romeiser, R., and W. Alpers (1997), An improved composite surface model for the radar backscattering cross section of the ocean surface: 2. Model response to surface roughness variations and the radar imaging of underwater bottom topography, *J. Geophys. Res.*, *102*, 25,251–25,267.

Romeiser, R., W. Alpers, and V. Wismann (1997), An improved composite surface model for the radar backscattering cross section of the ocean surface: 1. Theory of the model and optimization/validation by scatterometer data, *J. Geophys. Res.*, *102*, 25,237–25,250.

Sikora, T. D., and D. R. Thompson (2002), Air-sea turbulence statistics from synthetic aperture radar: An update, *Can. J. Remote Sens.*, *28*, 517–523.

Stoffelen, A., and D. L. T. Anderson (1993), ERS-1 scatterometer data characteristics and wind retrieval skill, in *Proceedings of First ERS-1 Symposium*, vol. 1, *ESA Publ. SP-359*, pp. 41–48, Eur. Space Agency, Paris, France.

Suess, M., S. Riegger, W. Pitz, and R. Werninghaus (2002), TerraSAR-X: Design and performance, paper presented at EUSAR 2002, VDE Conf. Off., Frankfurt, Germany.

Ufermann, S., and R. Romeiser (1999a), A new interpretation of multi-frequency/multipolarization radar signatures of the Gulf Stream front, *J. Geophys. Res.*, *104*, 25,697–25,706.

Ufermann, S., and R. Romeiser (1999b), Numerical study on signatures of atmospheric convective cells in radar images of the ocean, *J. Geophys. Res.*, *104*, 25,707–25,720.

Ulaby, F. T., R. K. Moore, and A. K. Fung (1986), *Microwave Remote Sensing: Active and Passive*, 3 vol., Addison-Wesley, New York.

Wadhams, P., V. Pavlov, J. Wilkinson, and B. Krogh (2002a), RV *Lance* cruise report, technical report, Project CONVECTION, Comm. of the Eur. Union, Brussels.

Wadhams, P., J. Holfort, E. Hansen, and J. P. Wilkinson (2002b), A deep convective chimney in the winter Greenland Sea, *Ice Clim. News*, *3*(1), 5–9.

A. Androssov, S. Kern, R. Romeiser, and A. Rubino, Institute of Oceanography, Center for Marine and Climate Research, University of Hamburg, Bundesstraße 53, 20146 Hamburg, Germany. (androssov@ifm.uni-hamburg.de; kern@ifm.uni-hamburg.de; romeiser@ifm.uni-hamburg.de; rubino@ifm.uni-hamburg.de)

L. Mitnik, Department of Satellite Oceanography, Pacific Oceanological Institute, Far Eastern Branch of the Russian Academy of Sciences, 43 Baltiyskaya Street, Vladivostok 690041, Russia. (mitnik@online.vladivostok.ru)

S. Ufermann, Laboratory for Satellite Oceanography, Southampton Oceanography Centre, European Way, Southampton, SO14 3ZH, UK. (ufermann@soton.ac.uk)

H. Wehde, Institute of Coastal Research, GKSS Research Center, Max-Planck-Straße 1, 21502 Geesthacht, Germany. (henning.wehde@gkss.de)